WILEY-VCH

Emerging Group-VI Elemental 2D Materials: Preparations, Properties and Device Applications

*Ziyuan Lin, Cong Wang, and Yang Chai**

Ziyuan Lin, Cong Wang, and Prof. Yang Chai
Department of Applied Physics, The Hong Kong Polytechnic University, Hung Hom, Kowloon, Hong Kong, China.
The Hong Kong Polytechnic University Shenzhen Research Institute, Shenzhen 518057, China.

E-mail: y.chai@polyu.edu.hk

Keywords: group-VI 2D materials, crystal structures, preparations, electrical properties, nanoelectronics

Due to the ultrathin thickness and dangling-bond-free surface, two-dimensional (2D) materials have been regarded as promising candidates for future nanoelectronics. In recent years, group-VI elemental 2D materials are rediscovered and found superior in electrical properties (*e.g.*, high carrier mobility, high photoconductivity and thermoelectric response). The outstanding semiconducting properties of group-VI elemental 2D enable the device applications including high-performance field-effect transistors and optoelectronic devices. The excellent environmental stability also facilitates fundamental studies and practical applications of group-VI elemental 2D materials. This review will first focus on the crystal structures of group-VI elemental 2D materials. Afterward, preparation methods for nanostructures of group-VI materials will be introduced with comprehensive studies. A briefly review on the electronic structures will then be presented with the understanding on the electrical properties. This review also contains the device applications of group-VI elemental 2D materials, emphasizing transistors, photodetectors and other appealing applications. Lastly, this review will provide the outlook for the development of group-VI elemental 2D materials, highlighting the challenges and opportunities in fundamental study and technological applications.

1. Introduction

Two-dimensional (2D) layered materials have been intensively investigated in the past decade, because they possess unique physical properties that are absent in bulk counterpart, and enable new promising applications.[1-7] The family of 2D materials is greatly enriched and becomes a large material catalogue consisting of graphene, hexagonal boron nitride (h-BN), transition metal dichalcogenides (TMDs), black phosphorous (BP), silicene, MXene, selenene (Se) and recently discovered tellurene (Te), *etc.*[8-13] These 2D materials have a layered or sheet-like structure with a thickness ranging from tenths of a nanometer (single atomic thickness) to tens of nanometer, while the lateral size can be up to micrometers or wafer scale. With different compositions and crystal structures, these 2D materials differ from each other in properties, offering wide range of material choices for diverse functionalities, including electronics, optoelectronics, sensors, energy conversion and storage.[14-21]

As Si transistors approach their scaling limit, the loss of gate electrostatic control on the nanoscale channel and the direct source-to-drain tunneling increase the off-state leakage currents, raise power dissipation, and thus severely degrade the performance of Si transistors.[22-25] Because of this scaling limit of Si transistors, exploration of new channel materials is of vital importance for future nanoelectronics. Due to the ultrathin thickness and dangling-bond-free surface, the emerging 2D materials are promising candidates for continuously downward scaling.[26] The diversity of 2D materials provides broad choices of semimetals (*e.g.*, graphene), insulators (*e.g.*, h-BN) and semiconductors (*e.g.*, TMDs, BP, Se, Te).[8-13] The 2D semiconductors with thickness-dependent bandgaps have been regarded as potential channel materials for replacing Si.[26] The layered nature of 2D semiconductors allows consistent thickness control with atomic precision down to the monolayer limit, leading to enhanced electrostatic control of the gate and further scaling of transistors. Also, the pristine surfaces of 2D semiconductors are free of dangling bonds even down to monolayer limit. The pristine surfaces can give rise to low density of interface trap states and consequently reduce the charge

scattering. Taking TMDs as an example, molybdenum disulfide (MoS_2), one of the most widely studied 2D semiconductors is a potential replacement for Si.[27-29] Based on theoretical calculation, 2D MoS_2 is predicted to have a direct source-to-drain tunneling leakage current two orders of magnitude smaller than that of Si.[22] For monolayer MoS_2, the leakage current will not limit the scaling of transistors down to one-nanometer gate length, which is superior to Si with a sub-five-nanometer scaling limit.[22] With the unique layer nature, 2D semiconductors alleviate the severe short channel effect. Therefore, 2D semiconductors have been regarded as potential options for transistors with ultimate thin channel.

After realizing advantages of 2D semiconductors over Si, numerous research studies focus on searching for 2D semiconductors with high carrier mobility and an appropriate band gap and exploring their usage in future nanoelectronics. In recent years, group-VI elemental 2D semiconductors including Se and Te, stand out for their simple composition and excellent properties, *e.g.*, higher carrier mobility than TMDs and better air stability than BP.[30-34] As two of the newest members of 2D materials, a few theoretical studies and experimental works have presented the intriguing electrical properties, *e.g.*, high carrier mobility, high photoconductivity and thermoelectric response, together with some appealing applications including high-performance field-effect transistors (FETs), optoelectronic devices and thermoelectric devices.[35-38] In this review, we intend to summarize the electrical properties and nanoelectronics applications of group-VI elemental 2D materials (Se and Te). We will begin with crystal phases and preparation methods before the brief review on the electronic structures and the resulting electrical properties. Afterward, we will emphasize the device applications; FETs, photodetector and other appealing applications, such as heterostructures. Lastly, we will provide our outlook for the development of group-VI elemental 2D materials, searching for exciting opportunities in fundamental study and technological applications.

2. Crystal structures of group-VI elemental 2D materials

The properties of 2D materials are not only related to their compositions but also strongly associated with the crystal structures, *i.e.,* how the atoms are arranged within the layer and how the layers are stacked. The understanding on crystal structures of 2D materials is essential for further studies and applications. For group-VI elemental 2D materials, various crystal phases of Se and Te have been theoretically proposed and examined, while only a few allotropes are experimentally synthesized and investigated.[39-46]

Figure 1(a) presents three structures of monolayer Se revealed by theoretical prediction: 1T-MoS_2-like structure (*t*-Se), tiled helical-chain structure (*c*-Se) and square structure (*s*-Se).[42] The *t*-Se phase has a 1T-MoS_2-like sandwiched structure, in which an individual layer consists of three layers of Se atoms, quite different from most elemental 2D materials.[47-49] The second *c*-Se phase is made up by a series of helical Se chains, which are parallel-arranged in a plane. The helical chains are stacked together by the weak interchain interactions. The structure of monoclinic *s*-Se has only 2 atoms in a unit cell, where one atom arranged at a corner of the square lattice and the other one is off the center of the square towards the corner direction. Theoretical calculations of electronic structure show that both *t*-Se and *c*-Se are indirect-band-gap semiconductors, while *s*-Se is predicted to exhibit semimetal property. Among these three Se crystal phases, the lowest formation energy of *c*-Se indicates the most stable phase is *c*-Se, which shares similar helical-chain structure with bulk Se. Although theoretical calculations show thermodynamic stability with three crystal phases, most experimentally prepared Se thin layers possess this *c*-Se crystal structure.[44, 50, 51]

Similar structural discrepancy is also predicted in Te. Qiao *et al.* reported detailed density functional theory (DFT) calculations on the crystal phases of 2D Te.[43] Under normal conditions, the *α*-phase Te with crystal structure in Figure 1(b) is the most stable phase for few-layer thickness, which is also confirmed experimentally.[43, 45] Few-layer Te shares the same trigonal crystal structure as bulk Te, in which individual helical chains of covalently bound Te atoms are parallel-aligned and oriented along the [001] direction. These chains are stacked

together by weak bonding. When the thickness is reduced to monolayer, the α-phase will transfer to more stable β-phase (Figure 1(c)), in which a Te helical chain moves towards the adjacent chain and forms an addition mirror symmetry. This different monolayer phase is experimentally confirmed by the epitaxial monolayer Te on highly oriented pyrolytic graphite (HOPG), of which the topographic image shows its in-plane lattice consistent with the predicted β-phase.[52] Another γ-phase Te as presented in Figure 1(d) is in analogy to the 1T-MoS_2 phase. It is expected to be transformed from α-phase to lower the energy of dangling bonds when the number of Te atoms in each chain is three, six or nine. Although α-phase is the most stable beyond monolayer thickness, the small energy difference among three crystal phases and the geometrical similarity may result in reversible phase transition α-β or α-γ by strain or doping engineering.[43]

Experimental results show that the group-VI elemental 2D materials with stable phases are c-Se and α-Te, both of which consist of helical chains.[39-41] These chains of Se or Te atoms are stacked together by weak bonding to form 2D nanosheets and 3D bulk. The weak interchain interactions in the crystal structure exists in two directions, which is quite different from conventional 2D materials with only weak interlayer interaction.[53] The structure anisotropy of Se and Te gives themselves a strong trend towards 1D growth or exfoliation, which brings some difficulties in preparing group-VI 2D materials.[40, 41] In addition, there is limited research investigation on the phase transition of other crystal phases of Se and Te with different properties from c-Se and α-Te. The structural discrepancy suggests the complexity of structure formation and transition mechanism, which is necessary for preparation and experimental investigation of other crystal phases.

3. Preparations of group-VI elemental 2D materials

To realize various applications of group-VI elemental 2D materials, it requires to develop reliable preparation approaches for large-area, high-yield and high-quality 2D samples. Due to

the structural anisotropy, Se and Te tend to follow 1D growth. Most of early research works dating back to last century reported multiple approaches to 1D structures of Se and Te. These synthesis methods have provided excellent references for recent development of growth methods for 2D Se and Te.[40, 54]

3.1. Solution synthesis for 1D structure

Solution synthesis offers feasible routes to free-standing Se and Te nanomaterials with high yield and relatively low reaction temperature. Gates *et al.* reported the synthesis of Se nanowires via solution method from the reaction in aqueous solutions of selenious acid and hydrazine by controlling the refluxing temperature.[55] The Se nanowires are successfully synthesized with diameters as small as 10 nm and lengths up to several hundred micrometers, as shown in **Figure 2**(a). Mayers *et al.* reported the reduction of orthotelluric acid or tellurium dioxide by hydrazine at various refluxing temperatures (90 ℃ to 200 ℃) to synthesize Te nanowires with spines, filaments, needles and tubular structures (Figure 2(b)).[56] In the synthesis of Se and Te by solution methods, the morphology control of 1D structures is achieved by different refluxing temperatures. To obtain 1D group-VI materials with high crystallinity, hydrothermal routes were proposed. Single crystalline Se nanobelts are reported to be synthesized through hydrothermal routes by reducing selenium dioxide with glucose at 160 ℃.[57] Revealed by time-dependent observation, the formation of Se nanobelts is governed by solid-solution-solid growth mechanism, involving initial formation of amorphous Se nanoparticles, partial dissolution of amorphous Se to recrystallize as nuclei and the final growth of nanobelts on the crystalline seeds costing the rest amorphous Se nanoparticles. Mo *et al.* also demonstrated a hydrothermal route by the disproportionation of sodium tellurite in aqueous ammonia at 180 ℃.[58] The as-synthesized Te nanobelts have an average thickness of 8 nm and a width of 30 to 500 nm. The hydrothermal process can be assisted by polymer surfactant like poly (vinyl alcohol) (PVA) and poly(vinyl pyrrolidone) (PVP). Uniform Se nanorod bundles have been synthesized with PVA capping agent by hydrothermal method.[59] With the assistance of PVP,

uniform Te nanowires with a diameter of 4-9 nm and nanobelts with a width of 250-800 nm are also prepared.[60] The selective synthesis of Te nanowires and nanobelts arises from different growth rates of crystal facets modulated by the amount of PVP.

Solution synthesis is also demonstrated for the preparation of Se-Te alloy or heterojunction. Mayers *et al.* reported the synthesis of monodisperse Se_xTe_y nanorods through the reduction of the mixture of selenious acid and orthotelluric acid by excess hydrazine in aqueous solution.[61] The compositions of Se_xTe_y alloy is controlled by the feeding ratio of Se and Te sources, which provides a simple preparation method for nanorods of Se-Te alloy with controllable compositions and tunable properties. Xu *et al.* offered a hydrothermal route to Se_xTe_{1-x}/Te/Se_xTe_{1-x} heterojunction nanorods through the reduction of sodium selenite and sodium tellurite by hydrazine hydrate.[62] The as-grown heterojunction nanorods exhibit a bone-like structure with Te-only middle part and two Se-Te alloy end segments. Careful control of pH value of the solution allows Te to crystallize prior to Se. The reduction of Se sources begins after the initial growth of pristine Te nanorods, resulting in the growth of Se_xTe_{1-x} at the two ends of the Te nanorods and the formation of alloy/semiconductor/alloy heterostructure. In recent year, Huang *et al.* reported a two-step synthesis for Te-Se heterojunction with core-shell structure.[63] The first-prepared Te nanotubes dispersion by hydrothermal synthesis was mixed with Se sources and reductant for Se growth on the surface of Te nanotubes. The obtained products are Te nanotubes with 60 nm diameters covered with Se wall with 20 nm thickness. Between the Te and Se interface, it is found that there is no formation of Te-Se bond.

Solution synthesis is a feasible route to Se and Te nanostructures, which relies on the reduction of Se/Te precursors. The easy composition modulation and low reaction temperature also facilitate the preparation of nanostructure of group-VI alloy and heterojunction. The formation of 1D Se/Te in solution synthesis is a homogeneous self-seeding process.[55, 56, 61] The nuclei are formed from the crystalline group-VI nanoparticles. The subsequent growth of nuclei complies with the structure anisotropy of Se/Te, which favors 1D growth. The addition of

polymer surfactant further confines the growth direction, bringing kinetic controls on the formation of 1D Se/Te.[57-60, 64-66] The reaction parameters, including temperature, pressure, surfactant and precursor concentration, have been investigated and revealed to determine the morphology of 1D structure of Se and Te, which achieves the uniform control over shape, thickness, width and length of group-VI nanomaterials.[55-58, 60, 64-67]

3.2. Vapor deposition for 1D structure

Vapor deposition has been an important method for growing low-dimensional material synthesis. Ren *et al.* reported a Se nanowire growth method through thermal evaporation by introducing Si powders.[68] The as-grown Se nanowires have several micrometers in length and 50~100 nm in diameter. During the growth process, the Si powders can react with Se vapor to form $SiSe_2$, which reduces the concentration of Se vapor transporting to the growth zone and prevents the formation of large Se bubbles on the growth substrates. As a result, the pristine Se nanowire growth is promoted with solid $SiSe_2$ remaining at the site of Si powders. In the meantime, Cao *et al.* proposed a vapor-liquid-solid (VLS) method to grow Se nanoribbons on Cu substrates.[69] The product consists of high-yield Se nanoribbons with average thickness of 15 nm, width of 50-300 nm and length of hundreds of micrometers. By controlling the deposition temperature (300 ℃) higher than the melting point of Se (~ 217 ℃), the growth begins with the gaseous Se aggregating into droplet shape on the substrate, followed by solidification via typical VLS process during natural cooling. Wang *et al.* demonstrated a vacuum physical vapor deposition (PVD) method to grow Se nanobelts on Si substrates without catalyst.[70] The as-prepared Se shows a nanobelt morphology with a 90 nm thickness and a 500-5000 nm width, as presented in Figure 2(c). The growth process was detected by time-dependent experiments. It is found that the Se growth experiences morphology evolution from nanospheres to nanorods, and then to the final nanobelts by agglomeration.

Vapor deposition has also been reported to produce 1D structure of Te. One of the very early studies demonstrated the growth of Te whiskers with a few micrometer lengths by direct

sublimation of solid Te. The morphology of Te whiskers is controlled by the substrate temperature.[71] As the substrate temperature rises, the shape of Te whiskers changes from spines to filaments and finally to needles. Similar PVD method is also demonstrated by Li *et al.*[72] Te tubes in a shape of hexagonal prisms with diameters ranging from ten to several hundred micrometers and length up to several centimeters are synthesized by simple evaporation of Te powder. The Te microtubes show a characteristic hollow structure, similar with rolled-up structure from 2D layer. The walls of Te microtubes are packed from Te spiral chains by weak interactions. The nucleation and growth processes with thermodynamic effect dominate the formation mechanism of Te tubes growths. The anisotropic structure is the primary reason for the formation of 1D structure, and the thermodynamic effect prefers exposed crystal facet with lowest surface free energy. The combination of both effects leads to the growth of Te tubes with hexagonal cross section. Except PVD, chemical vapor deposition (CVD) for Te is also demonstrated using Al_2Te_3 solid and H_2O vapor as precursors through chemical reaction in Ar atmosphere at 500 °C.[73] The H_2O vapor will react with the heated Al_2Te_3 powder and form H_2Te. The intermedia H_2Te will evaporate and decompose to Te vapor, which is directly deposited on the substrates at relatively low temperature. The as-prepared single-crystalline Te nanobelts (Figure 2(d)) have a thickness of about 10 to 20 nm, a width of 50 to 300 nm and a length up to tens of micrometers.

Most of reported vapor deposition of 1D group-VI materials involve the evaporation of Se or Te precursors; the transport of Se and Te vapor from sources with higher temperature to growth substrates with lower temperature; the solidification of Te vapor via VLS or vapor-solid (VS) process. The morphology of as-grown products is influenced by the growth parameters, including evaporation or reaction temperature, carrier gas flow rate and substrate temperature, which have been extensively investigated in the early studies.[68-75] The VLS or VS mechanisms govern the growth of Se and Te on the substrate. The nucleation begins at catalysts or initial droplets of Se and Te. The 1D growth is followed due to the structure anisotropy of Se and Te,

which tends to lower the energy of whole system. The understanding on 1D growth of Se and Te benefits development of vapor deposition for 2D Se and Te.

3.3. Growth of 2D structure

With the basis of early works on 1D Se and Te growth, solution synthesis and vapor deposition have been extended to 2D Se and Te growth.[44, 45, 76] Wang and co-works presented the solution synthesis of Te thin flakes through the reduction of sodium tellurite by hydrazine hydrate assisted with PVP ligand in an alkaline solution at 160 to 200 °C.[45] This technique provides a route to large-area, free-standing and high-quality 2D Te (**Figure 3**(a)). Figure 3(b) shows the micro-size Te flakes with a thickness of 10 nm. The thickness can be further reduced below 10 nm after a solvent-assisted post-growth thinning process by adjusting the pH value of dispersion solution, and monolayer, bilayer and trilayer Te are obtained. In the proposed solution synthesis, PVP concentration is of great importance to 2D growth of Te. The medium level of PVP as surfactant in growth can well adjust the growth rate at width and thickness direction, changing initial 1D growth to sequent 2D growth. As the schematic in Figure 3(c), the initial products are 1D nanostructures resulting from kinetic-driven 1D growth with PVP capping. As the reaction continues, the insufficient PVP capping will expose $\{10\bar{1}0\}$ surfaces with lowest free energy. The growth of $\{10\bar{1}0\}$ surfaces along $<12\bar{1}0>$ direction begins driven by thermodynamic effect, giving rise to intermedia Te. The simultaneous growth along $<12\bar{1}0>$ and <0001> directions leads to the formation of 2D Te. The transform from 1D growth to 2D growth is a result of balance between kinetic and thermodynamic effects.

Although solution synthesis successfully prepares 2D Te, it introduces impurities during complex chemical processes and fails to grow wafer scale 2D samples, which greatly limits its applications. Vapor deposition should be more potential for large-area and high-quality 2D group-VI materials. Peide D. Ye's group reported the preparation of Se thin flakes by PVD (Figure 3(d)) and post-growth transfer.[44] The as-grown Se sheets are distributed on the surface of polycrystalline Se films, as presented in Figure 3(e), which have a saw-like structure with

width of ~ 8 μm and length up to 50 μm. These sheets with average thickness of 15 nm are transferred to new substrates by Scotch tape for further device fabrication (Figure 3(f)). The growth of Se sheets is explained to be governed by VS mechanism. Time-dependent experiments reveal the morphology evolution from amorphous nanospheres to short nanorods on the polycrystalline films and finally to sheets on the films as the increasing deposition time. The growth mode changed from 1D to 2D is suggested to relate with the high chemical activity at the vertexes and ridges of short nanorods. When the end sites of nanorods are saturated during the growth, the Se vapor atoms will be absorbed on the surfaces of nanorods, which leads to growth along two directions <12$\bar{1}$0> and <0001> and turns nanorods to sheets. The growth of Te thin films is also realized by PVD with growth substrates at cryogenic temperatures.[76] Wafer-scale Te thin films with thickness varying from 8 to 30 nm and micro-size domains are obtained with a substrate temperature of -80 °C and -60 °C. The film quality is significantly influenced by the substrate temperatures (Figure 3(g) to (i)). The domain size is decreased from ~ 25 μm^2 to 3 μm^2 as the substrate temperature rises from -60 °C to -10 °C, as shown in Figure 3(j). The film will lose its uniformity and consist of small particles when the growth substrates are at room temperature (Figure 3(i)). Wang *et al.* also demonstrated the PVD method for hexagonal Te plates on the mica sheets (Figure 3(k)).[77] The obtained single-crystalline Te plates in Figure 3(k) have a thickness ranging from 30 to 80 nm with a few micrometers lateral size. The growth substrates, mica sheets have a surface free of dangling bond and resulting weak van der Waals interaction with Te, which promotes the migration of Te adatoms during deposition and facilitates the growth of Te plates without strict lattice mismatch. The growth of Te plates simply follows the Volmer-Weber model involving formation of Te nanoparticle, diffusion of Te adatoms and mergence into hexagonal structure (Figure 3(l)). The Te plates are distinguished from other reported 2D Te for the vertically aligned Te chains in plates. It is suggested to relate with the vertical sharp tips of Te nanoparticles, which serves as nuclei at the initial growth. In addition, CVD is reported to prepare 2D Te flakes. Zhang *et al.* developed

hydrogen-assisted CVD method as illustrated in Figure 3(m) and successfully grew ultrathin Te flakes on mica substrates.[78] The growth is realized by the reduction of tellurium dioxide in H_2 atmosphere. The as-prepared Te flakes exhibit triangular shape with thickness down to 5 nm (Figure 3(n) and 3(o)).

With intensive research efforts, bottom-up methods including vapor deposition and solution synthesis are successful to prepare 2D group-VI materials, although these methods are still underdeveloped compared with the growth of graphene and 2D TMDs.[53, 79-82] Solution synthesis can prepare large-area, high-quality, free-standing and single-crystalline thin flakes, which is suitable for high-performance device demonstration. The substrate-free growth also facilitates some applications like flexible electronics. However, the thickness variation limits large-scale applications, which requires further enhancement by delicate control of reaction parameters. The failure for wafer scale Te samples also hampers the application of solution synthesis in industry. Although vapor deposition is possible for wafer scale samples, the current status is far from satisfactory. The reported vapor deposition methods have been extended to 2D growth via delicate control on the growth parameters. However, the obtained single-crystalline Se/Te sheets and polycrystalline Se/Te thin film have relatively low quality. Compared with solution-synthesized products, the relatively small grain size and rough edges of vapor-deposited samples require necessary enhancement in quality (*e.g.,* purity, crystallinity and surface smoothness). Without detailed investigation on deposition parameters, the feasible and high-efficiency vapor deposition for large-scale, high-quality and single-crystalline 2D group-VI materials have not yet achieved, which is worth future exploration.

Apart from solution synthesis and vapor deposition, molecular beam epitaxy (MBE) provides high-quality production of 2D group-VI materials and atomic scale precise control on the thickness, which benefits the fundamental study on 2D group-VI materials. Atomically flat Te thin films are reported to be van der Walls epitaxially grown on graphene/6H-SiC(0001) substrates and HOPG by MBE.[52, 83] Monolayer Te films are successfully MBE-deposit on

HOPG by delicate control of reacting time, which is found to form different phase from few-layer and bulk Te. Although MBE combined with scanning tunneling microscopy (STM) can prepare and in-situ characterize pristine Te films, it suffers from the high cost, low efficiency and substrate limitation. Top-down methods like exfoliation also succeed in preparing 2D group-VI materials. Mechanical exfoliation by sliding a freshly cleaved facet of Te on SiO_2 substrates is reported, but the exfoliated Te with 15-nm thickness only has a width of 1-2 μm.[84] As the Te chains in bulk are bonded by weak interaction, they will break away from bulk vertically and laterally, forming thin and narrow belt-like structure, unlike other mechanical exfoliated 2D materials (graphene and TMDs) with large flat surface.[26, 85] Liquid exfoliation is another top-down method. The liquid-exfoliated Se nanosheets have an average thickness of 10-27 nm but the lateral size is only 40–124 nm.[51] The reported 5-nm-thick Te nanosheets by liquid exfoliation have very small lateral size in a range from 41.5 to 177.5 nm.[35] Although exfoliation methods offer routes to group-VI nanomaterials, the size of obtained 2D group-VI materials is quite small, which is extremely inappropriate for electronic device.

4. Electrical properties of group-VI elemental 2D materials

Before exploration of device applications of 2D group-VI material, it is important to understand their electrical properties. As emerging members of 2D materials, 2D Se and Te have received a few theoretical predictions and experimental studies on their electrical properties.[43, 83, 86-88]

Wang *et al.* conducted first principle calculations on the electrical properties of monolayer Se with 1T-MoS_2-like structure (denoted as *t*-Se in this review) and tiled helical-chain structure (denoted as *c*-Se).[86] As shown in **Figure 4**(a), the calculated band gap of *t*-Se and *c*-Se are 0.70 eV and 1.76 eV, which may be underestimated due to the calculation methods. The monolayer *t*-Se is predicted to possess high hole and electron mobilities, which are 9.48×10^3 $cm^2V^{-1}s^{-1}$ for hole and 6.97×10^3 $cm^2V^{-1}s^{-1}$ for electron. By comparison, the monolayer *c*-Se

has lower carrier mobility with anisotropic values. The calculated hole mobility of *c*-Se can reach 571 $cm^2V^{-1}s^{-1}$, which is comparable with the other conventional 2D materials (Figure 4(b)). Few-layer α-phase Te is also predicted to exhibit excellent semiconducting properties. In DFT calculation conducted by Qiao *et al.*,[43] bulk Te is found to have a nearly direct bandgap of 0.31 eV and the bandgap is expected to increase as the decrease of thickness. The thinnest α-Te has a predicted indirect bandgap of ~ 0.9 eV. As the thickness increases, the valence band maximum (VBM) shifts from -4.98 to -4.35 eV, and the conduction band minimum (CBM) changes slightly, suggesting *p*-type contact of bilayer α-Te with most of metals (Figure 4(c)). The thickness-dependent bandgap of 2D Te has been experimentally revealed by scanning tunneling spectroscopy (STS). MBE offers high-quality epitaxial Te films with precise control on layer number. The bandgaps are determined by STS for bilayer (0.85 eV), trilayer (0.74 eV) and 13-layer (0.49 eV) Te, in agreement with the DFT calculations.[83] The bandgap of monolayer Te (β-Te) is measured to be 0.92 eV.[83] Another crystal phase of 2D Te, γ-Te is also predicted as a semiconductor with indirect bandgap of 0.76 eV.[30] The extraordinarily large carrier mobility in 2D Te is expected 10^4-10^6 $cm^2V^{-1}s^{-1}$ for hole and 10^3-10^4 $cm^2V^{-1}s^{-1}$ for electron, appreciably larger than that of 2D TMDs and few-layer BP.[43, 49, 89-91] The mobility values also exhibit anisotropy due to the structure anisotropy.[43] The thickness-dependent bandgap and large carrier mobility of 2D Se and Te make 2D group-VI materials promising 2D semiconducting channels and facilitate their applications in FET devices.

To evaluating the possibility of application in photodetectors, Qiao *et al.* presented the understanding on optoelectronic properties of 2D Te.[43] DFT calculation presents the relatively high absorbance for normal incident light (~ 9% at 3.2 eV), which is larger than that of BP.[49] It is interesting to notice that the light absorption exhibits almost isotropy with bilayer to 5-layer thickness despite the structure anisotropy, and slightly restores anisotropy at 6-layer or thicker Te (Figure 4(d)). The energy of absorption edge is about 0.2 eV larger than the predicted bandgap, suggesting inter-band transition and carrier transfer in 2D Te. These predicted features

indicate great potential of Te in optical applications, which still requires detailed experimental investigation. Optical characterizations like Raman can easily identify the in-plane anisotropic properties of 2D group-VI materials. Figure 4(e) depicts Raman spectra evolution with polarized incident laser in different directions. The intensity changes of two Raman active modes, E1 and A1, are recorded when the angle between crystal orientation and light polarization evolves from -90º to 90º.[44] Similar angle-resolved Raman spectra is also observed in 2D Te.[45] The A_1 mode of 2D Te exhibits the largest sensitivity to orientation angles between the [0001] direction of 2D Te and the polarization of the excitation laser. The angle-resolved Raman can help the orientation determination of 2D group-VI materials by the peak evolution, confirming the anisotropic properties of 2D group-VI materials.

Thermoelectric effect enables a direct conversion between heat and electricity, which not only can be applied in photodetection but also facilitate energy harvesting. The figure of merit zT, which determines the performance of a thermoelectric material, equals to $S^2\sigma T/\kappa$, where S is the Seebeck coefficient, σ is the electrical conductivity and κ is the thermal conductivity. Group-VI materials have received some attentions owing to the excellent thermoelectric property.[33, 92-94] Lin *et al.* reported theoretical thermoelectric property of 2D Se.[33] The 2D Se exhibits better thermoelectric property by *n*-doping with maximum zT reaching 0.64 at the moderate dopant concentration of 2×10^{12} cm^{-2}. Peng *et al.* investigated thermoelectric property of Te by DFT. The calculation presents the optimum zT is 0.31 at room temperature with hole concentration around 10^{19} cm^{-3}.[92] Lin *et al.* extracted the actual zT of Te samples by transport property measurement.[93] The electronic structure of Te leads to a high power factor ($S^2\sigma$). With reasonably low thermal conductivity, Te shows a remarkably high figure of merit of ~1.0 at about 500K with the carrier concentration of 2.65×10^{19} cm^{-3}, higher than other thermoelectric materials (Figure 4(f)). The excellent thermoelectric properties of group-VI materials suggest the great potential in energy harvesting and infrared photodetection, *etc*.

Compared with few-layer BP with environmental instability, 2D group-VI materials shows their superiority in great air-stability. The calculation shows the sufficient reaction energy barrier (0.85~0.94 eV) to prevent the oxidation of Te at atmosphere, suggesting the environmental stability of Te.[43] The stability is also experimentally confirmed by the performance retention of FETs based on 2D group-VI materials.[44, 45] Figure 4(g) and 4(h) show the excellent stability of device performance of FETs based on 2D Se and Te after air exposure for 15 days and 55 days, respectively. The excellent environmental stability of 2D group-VI materials is critical for the fundamental studies and practical applications.

5. Device applications of group-VI elemental 2D materials

The unique electrical properties of 2D group-VI materials enable the exploration of device applications including FETs and photodetectors, holding the great potentials for high-performance 2D materials based electronic devices.

5.1. FETs

Transistors are fundamental building blocks for integrating circuits, which are widely used in modern electronic devices. The 1D structure of Se has been utilized as channel materials in early research study.[95] The FETs based on Se nanobelts with 20 to 90 nm thickness present *p*-type electrical conduction with hole mobility of 0.63 $cm^2V^{-1}s^{-1}$ and carrier concentration of 9.35 × 10^{16} cm^{-3}. The *p*-type characteristic is predicted to be associated with the different terminations of contaminations on the Se surface. Recently, Qin *et al.* reported back-gated FETs based on 16-nm-thick 2D Se nanosheet prepared by PVD and post-grown transfer.[44] The Se FET with Ni/Au contacts exhibits typical *p*-type transport property with high ON/OFF ratio over 10^6 but low hole mobility of 0.26 $cm^2V^{-1}s^{-1}$ (**Figure 5**(a)). The ON-state current is relatively low with the maximum value of about 20 mA/mm at a drain voltage of 3 V. The field-effect mobility is much lower than the theoretical value (571 $cm^2V^{-1}s^{-1}$),[86] which possibly results from poor quality of nanosheet samples. The surface contaminations formed during

device fabrication process can also lead to the poor performance, which deserves further improvement.

In contrast, the Te FETs exhibit impressive electrical performance. Wang *et al.* demonstrated the first FETs based on few-layer Te flakes prepared by solution synthesis.[45] As shown in Figure 5(b), the device with Pd contacts and 7.5-nm-thick 2D Te channel presents outstanding *p*-type characteristic with high ON/OFF ratio of 10^5 and large drain current of 300 mA/mm. The thickness-dependent field-effect hole mobility (Figure 5(c)) shows a maximum value of 700 $cm^2V^{-1}s^{-1}$ for 16-nm-thick Te flakes at room temperature. The drain current can be further increased to record-high value of 1 A/mm by scaling down the channel length to 300 nm and utilizing ALD-grown high-κ dielectric. Ren *et al.* also presented high-performance electrolyte-gated FETs based on solution-synthesized Te flakes.[37] The electrolyte gating efficiently tunes the charge-dependent properties of 2D Te, achieving charge density over 10^{13} cm^{-2} and mobility higher than 500 $cm^2V^{-1}s^{-1}$. The temperature-dependent electrical measurement revealed the 2D insulator-metal transition of Te that is realized by tuning gate voltage. The high performance of devices based on solution-synthesized Te is greatly related with the high-quality and single-crystalline Te flakes for device channels. The 2D Te samples prepared by vapor deposition are also utilized for FET fabrication. Zhang *et al.* reported FET fabrication with CVD-grown Te flakes.[78] In ambient condition, the Te FETs with *p*-type transport property have a small ON/OFF ratio of ~ 10 and a low hole mobility of ~ 2.5 $cm^2V^{-1}s^{-1}$. Zhao *et al.* also reported *p*-type FETs fabricated with PVD-grown Te films as channels.[76] The device structure consists of Ni metal contacts and 5-nm-thick ZrO_2 gate dielectric. The FET with 8-nm-thick Te exhibits ON/OFF ratio of ~10^4, an effective hole mobility of ~35 $cm^2V^{-1}s^{-1}$ and subthreshold swing (SS) of 108 mV/dec at room temperature. Similar thickness-dependent mobility is observed and the effective mobility for 16-nm-thick Te is 140 $cm^2V^{-1}s^{-1}$, lower than that of 2D Te with same thickness prepared by solution synthesis. Benefiting from the wafer-scale and uniform Te thin film by PVD, Zhao and co-workers also demonstrated integrated circuits based on Te FETs.[76]

A Te based full-adder (Figure 5(d)) consisting of 9 NANDs and 4 inverters was fabricated with a total number of 35 Te transistors (Figure 5(e)). A multiplier circuit with 39 Te transistors was also constructed, which successfully realizes multiplication functions with a maximum output voltage loss of 3% (Figure 5(f) and 5(g)). To further explore the application of 2D Te in integrated circuits, complicated 3D logic gates, specifically, two-layer inverters based on *p*-type Te FETs were fabricated (Figure 5(h)). The inverter achieves the NOT function with a gain of about 12 at V_{dd} = 2 V (Figure 5(i)). The demonstration of integrated circuits indicates great potential of large-scale applications of 2D group-VI materials. Compared with figures of merit of FETs based on 2D Te by solution synthesis, the poorer performance of individual FET with 2D Te by vapor deposition (PVD and CVD) suggests the low quality of vapor-deposited samples. However, vapor deposition is more potential for wafer-scale samples and consequently facilitates large-scale applications. We believe that the development of vapor deposition methods can improve the quality (*e.g.* purity, crystallinity and smoothness) of 2D group-VI materials and enhance the device performance of FETs based on 2D group-VI materials.

In addition, metal contact is another critical factor influencing the device performance.[96, 97] Most of reported FETs based on 2D group-VI materials exhibits *p*-type characteristic, which results from the high level of VBM of 2D group-VI materials.[43] The metal contacts with high work function lying below the VBM of 2D group-VI materials facilitates the hole transport in the channel, giving rise to small barrier height for hole and high field-effect hole mobility. Yan *et al.* theoretically examined the interfacial characteristics between monolayer Te and common bulk metals.[98] It is predicted that lateral *p*-type Schottky contact is formed with Cu, Ni, Ag, Pt and Pd due to Fermi level pinning and lateral *n*-type Schottky contact is formed with Sc. There are limited experimental studies on the contact engineering of 2D group-VI materials, which is worth further investigation to enhance device performances.

5.2. Photodetectors

Photodetectors are another potential device application for 2D group-VI materials. Qin *et al.* fabricated phototransistors based on Se nanosheets (**Figure 6**(a)).[44] The devices exhibit pronounced photo-response under different illumination power densities even down to 0.21 mW/cm^2. To evaluate the performance of the phototransistors, photoresponsivity was calculated to be 263 A/W at 0.21 mW/cm^2 illumination power density, higher than that of other reported 2D materials.[85, 99, 100] The responsivity and photocurrent are linearly proportional to the illumination power, suggesting the photoconductive effect contributes to the photocurrent generation (Figure 6(b)). Chang *et al.* also demonstrated self-powered photodetectors based on Se microtubes by asymmetric contacts. The devices consist of Ag metal on one side of Se and In-Ga alloy on the other side, forming Schottky junction photodetectors.[101] The built-in electric field at the In-Ga/Se Schottky junction interface can effectively separate photogenerated carriers in Se, contributing to large photocurrent. The devices exhibit a broad photo response in the wavelength ranging from 300 to 800 nm with short response/decay time (Figure 6(c)). The high responsivity (408 mA/W under 532 nm) and detectivity (1.30×10^{13} Jones under 532 nm) are achieved for the Se based photodetector, suggesting great potential of Se in photodetectors. Wang *et al.* fabricated photodetectors based on Te plates on the mica substrates directly after the growth.[77] A pronounced photo response is observed when the device is illuminated by 473 nm laser (Figure 6(d)), which is sustained after the bending of flexible substrates. The photoresponsivity can reach 389.5 A/W, suggesting the promising application of 2D Te in optoelectronic devices. Amani *et al.* presented short-wave infrared (SWIR) photodetectors with solution synthesized 18-nm-thick Te flakes as channel.[102] An optical cavity with optically thick Au and Al_2O_3 dielectric spacer layer was utilized to increase the absorption (Figure 6(e)). The device exhibits high responsivities over the entire SWIR range with a cutoff wavelength of 3.4 μm. The responsivity is dependent on Al_2O_3 thickness and gate voltage with a peak value of 16 A/W at room temperature (Figure 6(f)). The peak specific detectivity was measured to be 2.9×10^9 $cmHz^{1/2}W^{-1}$. In addition, the thermoelectric effect of Te can contribute the

photocurrent generation.[93] Qiu *et al.* studied the thermoelectrical current in Te flakes stimulated by local laser heating.[103] The device follows conventional phototransistor structure. As schematically shown in Figure 6(g), when the laser illuminates one side of 2D Te, the local temperature of this side will be higher than the other, which will create carrier concentration gradient and diffusion current flows. The short circuit thermoelectric current mapping (Figure 6(h)) shows that the current can reach 3 μA with an incident laser power of 3 mW. It is also found that the contacts with high work function can help to efficiently collect thermoelectrically generated carriers.

The reported photodetectors based on Se/Te indicate the great potential 2D group-VI materials in optoelectronic applications.[39, 40, 51, 77, 78, 102, 103] The photocurrent generation mechanisms of 2D group-VI materials can be roughly classified as photoconductive effect (PCE), photovoltaic effect (PVE) and photothermoelectric effect (PTE).[104] PCE and PVE are associated with the excitation of free carriers caused by illumination. In PCE, the photoinduced free carriers are separated by the external applied voltage, which forms the photocurrent. The increased carrier concentration caused by light excitation reduces the resistance of semiconductor channels, which leads to larger light current (I_{light}) than dark current (I_{dark}) at the same applied bias. The photocurrent is extracted to be $I_p = I_{light} - I_{dark}$. For PVE, the photocurrent is generated due to the separation of photogenerated electron-hole pairs by the built-in electric field of *p-n* junction or Schottky junction at the contacts. The built-in electric field can be achieved by heterostructures, doping and asymmetric contacts, *etc*. Under illumination with photon energy larger than band gap, the excited electron-hole pairs are separated by the built-in electric field, forming the short-circuit current. When the circuit is open, the separated pairs will be accumulated at the opposite ends of devices, forming open-circuit voltage. By comparison, PTE is related to the thermal effect of the materials induced by light irradiation. The local heating by light illumination results in a temperature gradient at the semiconductor channel, which consequently causes the carrier concentration gradient. As a result, the different

carrier densities give rise to diffusion current flow. The thermoelectric voltage induced by PTE is related with the Seebeck coefficients of the channels. These photocurrent generation mechanisms indicate that Se and Te have potential for high-performance photodetectors and various optoelectronic applications.

5.3. Heterostructures

Pristine Se and Te have presented their potential applications in nanoelectronics. The alloy of group-VI materials and heterostructures are also received attentions for their interesting properties.[61, 105, 106] Liu *et al.* investigated group-VI compounds by first-principles calculations.[105] The stability of two monolayer group-VI compounds, α-Se_2Te (**Figure 7**(a)) and α-$SeTe_2$ (Figure 7(b)), were theoretically confirmed, both of which possess 1T-MoS_2-like structure. The detailed calculations reveal that monolayer α-Se_2Te is a semiconductor with indirect band gap of 0.38 eV while monolayer α-$SeTe_2$ is a direct-gap semiconductor with band gap of 0.33 eV. The carrier mobilities in these two alloys can reach 5400 $cm^2V^{-1}s^{-1}$. Although the Se_xTe_y alloy has been prepared by mixture of Se and Te precursor,[61] the experimental investigation on the properties of group-VI compounds and the corresponding device applications have not yet been conducted. Except compound alloys, the heterostructures with 2D group-VI materials are also demonstrated. Chen *et al.* reported 1D/2D hybrid structure of Se prepared by plasma-assisted growth,[106] which achieved broad photo-response in the wavelength ranging from ultraviolet (405 nm) to infrared (1550 nm). The phototransistors based on 1D nanowires array/2D thin film hybrid structure of Se exhibits I_{on}/I_{dark} current ratio up to 700 with responsivity of 6 mA/W and fast photo response in 25 ms (Figure 7(c)). Huang *et al.* also presented photoelectrochemical (PEC)-type photodetection in Se-Te heterojunction. The two-step solution synthesis prepares Te nanotube covered with Se forming Se-Te nanotube with heterojunction at the interface.[63] The photo response is achieved under simulated light in KOH solution with photoresponsivity of 98.8 μA/W. As Figure 7(d) shows, the built-in electric field of Se-Te heterojunction allows the self-powered photo-response in junction photodetectors,

which is absent in pristine Se or Te photodetectors. The 2D group-VI materials also can form heterostructures with other 2D materials (*e.g.* graphene, TMDs). Yan *et al.* predicted graphene electrodes can form lateral *p*-type Ohmic contact with monolayer Te, resulting from weak Fermi level pinning effect and the work function match with the VBM of 2D Te.[98] The Te/TMDs heterojunction is also studied. The prediction reveals that 2D Te and TMDs form desirable type II band alignment with strong charge separation and enhanced sunlight absorption, which is suitable for fabrication of heterojunction solar cells.[107] The maximum power conversion efficiency of heterojunction solar cells can reach 22.5% for Te/WTe_2 heterostructure (Figure 7(e)), which is competitive over other reported 2D heterojunction solar cells. Qin *et al.* reported experimental demonstration of Se/ReS_2 heterostructure.[108] The Se nanoplates are epitaxially grown on ReS_2 flakes by two-step vapor deposition. The phototransistors fabricated with Se/ReS_2 heterostructure (Figure 7(f)) present photo-response from 322 nm to 633 nm wavelength (Figure 7(g)) with fast response time less than 10 ms. The maximum photoresponsivity is 36 A/W under 370 nm light illumination with 0.03 mW/cm^2 power density (V_{ds} = 3 V and V_g = 0 V). The photocurrent is generated due to the fast transfer of photogenerated electrons from Se nanoplates to the underlying ReS_2 flakes. The quasi-1D structure of group-VI materials also benefit mixed-dimensional heterostructures, which provide additional approaches for electronic devices based on group-VI materials. Qin *et al.* demonstrated a dual-channel phototransistor based on 1D Se/2D ReS_2 heterostructures.[109] Compared with bare ReS_2-based devices, the heterostructure photodetector exhibits significant enhancement with the responsivity up to 98 A/W at 400 nm light with power intensity of 1.7 mWcm^{-2} and fast response speed with rise time in 45 ms. Similar Se/InSe heterostructure is reported by Shang *et al*.[110] The self-powered photodetectors based on Se/InSe heterostructure exhibit high responsivity ranging from the UV to visible region. The responsivity can reach 110mA/W at zero bias under 460 nm light. The 1D Te is also reported to form heterostructures with 2D InSe.[111] The Te/InSe devices achieve ultrasensitive and broadband photo response

with a high I_{on}/I_{dark} current ratio over 10^4 and a comparable responsivity of 0.45 A/W at visible light illumination with weak incident power. Although with much experimental reports, the understandings on alloy or heterostructure of 2D group-VI materials are still indistinct, which hinders the development of intriguing applications based on the alloy and heterostructure of 2D group-VI materials.

6. Conclusions and outlooks

Despite being one of the newest members in 2D materials family, 2D group-VI materials (Se and Te) have shown intriguing properties and great technological potential. In this review, we summarized the crystal structures, preparation methods, electrical properties and promising applications of 2D group-VI materials. The common structure of 2D group-VI materials consists of helical chains stacked together by weak bonding, which brings strong structure anisotropy, as well as strong tendency of 1D growth and in-plane anisotropy of electrical properties. Solution synthesis and vapor deposition have been developed for high-quality and large-scale 2D group-VI materials. The 2D group-VI materials distinguish themselves from other 2D semiconductors (*e.g.,* TMDs and BP) for their superior electrical properties. The extremely large predicted carrier mobility is much higher than that of TMDs and BP, facilitating the device applications of 2D group-VI materials. Compared with some other elemental 2D materials like BP and silicene, 2D Se and Te possess excellent environmental stability. Some device applications have been demonstrated with 2D group-VI materials, exhibiting high performance and indicating the great potential of 2D group-VI materials in future nanoelectronics.

The recent investigations on 2D group-VI materials open up new challenges and opportunities for development of 2D group-VI materials. Preparation method is one of the most challenging problems. Solution synthesis provides a way for high-quality and single-crystalline 2D group-VI materials. However, the large-scale or wafer-scale growth relies on vapor

deposition, which is necessary for wafer-scale applications like integrated circuits. The devices fabricated with vapor-deposited samples exhibit poorer performance compared with devices based on solution-synthesized samples, which results from the relatively low quality of 2D group-VI materials prepared by vapor deposition. Therefore, vapor deposition requires necessary improvement to enhance the quality of wafer-scale products (*e.g.,* purity, crystallinity and surface smoothness), which further facilitates the wafer-scale industrial applications (*e.g.,* integrated circuits) of 2D group-VI materials.

Although the recent device demonstrations have shown the promising applications of 2D group-VI materials in nanoelectronics, the carrier dynamics and transport mechanisms in 2D group-VI materials are not received thorough understanding compared to other 2D semiconductors. The extensively reported FETs based on 2D group-VI materials exhibit *p*-type transport property due to the high level of VBM of 2D group-VI materials and the Fermi level pinning effect at the contacts. To realize low-power complementary circuits, it is important to fabricate both *p*-type and *n*-type FETs with the same channel materials. There are several approaches including contact engineering, doping engineering and interface engineering which can modulate carrier transport in 2D channels and achieve polarity control, performance improvement and novel application extension. These approaches require understanding on carrier transport behavior in 2D group-VI materials, which is worth future research investigation.

The 2D heterostructures provide unprecedented possibilities for novel applications by stacking different 2D materials sequentially. Band alignments and charge transfer at the interfaces determine the appealing properties of 2D heterostructures, which demands profound understandings. However, the heterostructures between 2D group-VI materials and other 2D materials are rarely reported in experiment. The development of heterostructures with 2D group-VI materials can extend their applications to other fields such as tunneling devices and heterojunction solar cells.

Most of experimentally reported 2D group-VI materials have structures of helical chains. Theoretical predictions have presented some different crystal phases with thermodynamic stability, which exhibit different properties from the common structure of 2D group-VI materials. However, allotropes growth and phase transition of 2D group-VI materials receive very limited research investigation. The complicated structure formation and transition mechanism are still waiting to be disclosed.

In conclusion, 2D group-VI materials are fascinating materials due to their excellent properties and great potential in nanoelectronics. As the emerging members in 2D materials family, 2D group-VI materials faces some significant challenges, including preparation methods improvement and carrier transport understanding, which requires continuing research investigation. It is anticipated that more comprehensive understanding on 2D group-VI materials can be developed with concerted efforts.

Acknowledgements

This work is supported by the Research Grant Council of Hong Kong (PolyU 152053/18E) and The Project Supported by Shenzhen Science and Technology Innovation Commission (JCYJ20180507183424383).

Received: ((will be filled in by the editorial staff))
Revised: ((will be filled in by the editorial staff))
Published online: ((will be filled in by the editorial staff))

References

[1] K.S. Novoselov, A.K. Geim, S.V. Morozov, D. Jiang, Y. Zhang, S.V. Dubonos, I.V. Grigorieva, A.A. Firsov, *science*. **2004**, 306, 666-669.

[2] K.S. Novoselov, A.K. Geim, S. Morozov, D. Jiang, M.I. Katsnelson, I. Grigorieva, S.

Dubonos, Firsov, AA, *nature*. **2005**, 438, 197-200.

[3] A. Cresti, N. Nemec, B. Biel, G. Niebler, F. Triozon, G. Cuniberti, S. Roche, *Nano Research*. **2008**, 1, 361-394.

[4] S. Bai, L. Wang, X. Chen, J. Du, Y. Xiong, *Nano Research*. **2015**, 8, 175-183.

[5] E.H. Cho, W.G. Song, C.J. Park, J. Kim, S. Kim, J. Joo, *Nano Research*. **2015**, 8, 790-800.

[6] X. Wang, L. Huang, Y. Peng, N. Huo, K. Wu, C. Xia, Z. Wei, S. Tongay, J. Li, *Nano Research*. **2016**, 9, 507-516.

[7] Z. Lin, C. Liu, Y. Chai, *2D Materials*. **2016**, 3, 041009.

[8] Z. Lin, L. Cai, W. Lu, Y. Chai, *Small*. **2017**, 13, 1700051.

[9] S. Liu, N. Huo, S. Gan, Y. Li, Z. Wei, B. Huang, J. Liu, J. Li, H. Chen, *Journal of Materials Chemistry C*. **2015**, 3, 10974-10980.

[10] X. Zhang, Z. Lai, Q. Ma, H. Zhang, *Chemical Society Reviews*. **2018**, 47, 3301-3338.

[11] D. Geng, H.Y. Yang, *Advanced Materials*. **2018**, 30, 1800865.

[12] L. Pi, L. Li, K. Liu, Q. Zhang, H. Li, T. Zhai, *Advanced Functional Materials*. **2019**, 29, 1904932.

[13] F. Matusalem, M. Marques, L.K. Teles, F. Bechstedt, *Physical Review B*. **2015**, 92, 045436.

[14] Z. Lin, J. Wang, X. Guo, J. Chen, C. Xu, M. Liu, B. Liu, Y. Zhu, Y. Chai, *InfoMat*. **2019**, 1, 242-250.

[15] K. Xu, Y. Zhao, Z. Lin, Y. Long, Y. Wang, M. Chan, Y. Chai, *Semiconductor Science and Technology*. **2017**, 32, 124002.

[16] Q. Wang, C. Zhou, Y. Chai, *Nanoscale*. **2020**, 12, 8109-8118.

[17] Y. Zhang, F. Zhang, Y. Xu, W. Huang, L. Wu, Y. Zhang, X. Zhang, H. Zhang, *Advanced Functional Materials*. **2019**, 29, 1906610.

[18] N. Huo, G. Konstantatos, *Advanced Materials*. **2018**, 30, 1801164.

[19] W. Gao, Z. Zheng, P. Wen, N. Huo, J. Li, *Nanophotonics*. **2020**, 1, ahead-of-print.

[20] W. Tao, N. Kong, X. Ji, Y. Zhang, A. Sharma, J. Ouyang, B. Qi, J. Wang, N. Xie, C. Kang,

Chemical Society Reviews. **2019**, 48, 2891-2912.

[21] H. Yang, Y. Ma, Y. Liang, B. Huang, Y. Dai, *ACS applied materials & interfaces*. **2019**, 11, 37901-37907.

[22] S.B. Desai, S.R. Madhvapathy, A.B. Sachid, J.P. Llinas, Q. Wang, G.H. Ahn, G. Pitner, M.J. Kim, J. Bokor, C. Hu, *Science*. **2016**, 354, 99-102.

[23] M. Lundstrom, *Science*. **2003**, 299, 210-211.

[24] H. Kawaura, T. Sakamoto, T. Baba, *Applied Physics Letters*. **2000**, 76, 3810-3812.

[25] W.-S. Cho, K. Roy, *IEEE Electron Device Letters*. **2015**, 36, 427-429.

[26] J. Kang, W. Cao, X. Xie, D. Sarkar, W. Liu, K. Banerjee, *Proc. SPIE.* **2014**, 9083, 908305.

[27] Y. Yoon, K. Ganapathi, S. Salahuddin, *Nano letters*. **2011**, 11, 3768-3773.

[28] H. Wang, L. Yu, Y.-H. Lee, Y. Shi, A. Hsu, M.L. Chin, L.-J. Li, M. Dubey, J. Kong, T. Palacios, *Nano letters*. **2012**, 12, 4674-4680.

[29] J. Kang, W. Liu, K. Banerjee, *Applied Physics Letters*. **2014**, 104, 093106.

[30] Z. Zhu, X. Cai, S. Yi, J. Chen, Y. Dai, C. Niu, Z. Guo, M. Xie, F. Liu, J.-H. Cho, *Physical review letters*. **2017**, 119, 106101.

[31] A. Apte, E. Bianco, A. Krishnamoorthy, S. Yazdi, R. Rao, N. Glavin, H. Kumazoe, V. Varshney, A. Roy, F. Shimojo, *2D Materials*. **2018**, 6, 015013.

[32] Z. Zhu, C. Cai, C. Niu, C. Wang, Q. Sun, X. Han, Z. Guo, Y. Jia, *arXiv preprint arXiv:1605.03253*. **2016**.

[33] C. Lin, W. Cheng, G. Chai, H. Zhang, *Physical Chemistry Chemical Physics*. **2018**, 20, 24250-24256.

[34] Y. Du, G. Qiu, Y. Wang, M. Si, X. Xu, W. Wu, P.D. Ye, *Nano letters*. **2017**, 17, 3965-3973.

[35] Z. Xie, C. Xing, W. Huang, T. Fan, Z. Li, J. Zhao, Y. Xiang, Z. Guo, J. Li, Z. Yang, *Advanced Functional Materials*. **2018**, 28, 1705833.

[36] S. Deckoff-Jones, Y. Wang, H. Lin, W. Wu, J. Hu, *ACS Photonics*. **2019**, 6, 1632-1638.

[37] X. Ren, Y. Wang, Z. Xie, F. Xue, C. Leighton, C.D. Frisbie, *Nano letters*. **2019**, 19, 4738-

4744.

[38] W. He, H. Van Ngoc, Y.T. Qian, J.S. Hwang, Y.P. Yan, H. Choi, D.J. Kang, *Applied Surface Science*. **2017**, 392, 1055-1061.

[39] N.R. Glavin, R. Rao, V. Varshney, E. Bianco, A. Apte, A. Roy, E. Ringe, P.M. Ajayan, *Advanced Materials*. **2020**, 32, 1904302.

[40] S. Chaudhary, S. Mehta, *Journal of nanoscience and nanotechnology*. **2014**, 14, 1658-1674.

[41] W. Wu, G. Qiu, Y. Wang, R. Wang, P. Ye, *Chemical Society Reviews*. **2018**, 47, 7203-7212.

[42] C. Liu, T. Hu, Y. Wu, H. Gao, Y. Yang, W. Ren, *Journal of Physics: Condensed Matter*. **2019**, 31, 235702.

[43] J. Qiao, Y. Pan, F. Yang, C. Wang, Y. Chai, W. Ji, *Science bulletin*. **2018**, 63, 159-168.

[44] J. Qin, G. Qiu, J. Jian, H. Zhou, L. Yang, A. Charnas, D.Y. Zemlyanov, C.-Y. Xu, X. Xu, W. Wu, *ACS nano*. **2017**, 11, 10222-10229.

[45] Y. Wang, G. Qiu, R. Wang, S. Huang, Q. Wang, Y. Liu, Y. Du, W.A. Goddard, M.J. Kim, X. Xu, *Nature Electronics*. **2018**, 1, 228-236.

[46] C. Wang, X. Zhou, J. Qiao, L. Zhou, X. Kong, Y. Pan, Z. Cheng, Y. Chai, W. Ji, *Nanoscale*. **2018**, 10, 22263-22269.

[47] V. Kochat, A. Samanta, Y. Zhang, S. Bhowmick, P. Manimunda, S.A.S. Asif, A.S. Stender, R. Vajtai, A.K. Singh, C.S. Tiwary, *Science advances*. **2018**, 4, e1701373.

[48] S. Mardanya, V.K. Thakur, S. Bhowmick, A. Agarwal, *Physical Review B*. **2016**, 94, 035423.

[49] J. Qiao, X. Kong, Z.-X. Hu, F. Yang, W. Ji, *Nature communications*. **2014**, 5, 1-7.

[50] T. Fan, Z. Xie, W. Huang, Z. Li, H. Zhang, *Nanotechnology*. **2019**, 30, 114002.

[51] C. Xing, Z. Xie, Z. Liang, W. Liang, T. Fan, J.S. Ponraj, S.C. Dhanabalan, D. Fan, H. Zhang, *Advanced Optical Materials*. **2017**, 5, 1700884.

[52] J. Chen, Y. Dai, Y. Ma, X. Dai, W. Ho, M. Xie, *Nanoscale*. **2017**, 9, 15945-15948.

[53] R. Kumar, S. Sahoo, E. Joanni, R.K. Singh, R.M. Yadav, R.K. Verma, D.P. Singh, W.K. Tan, A.P. del Pino, S.A. Moshkalev, *Nano Research*. **2019**, 12, 2655–2694.

[54] Z. He, Y. Yang, J.-W. Liu, S.-H. Yu, *Chemical Society Reviews*. **2017**, 46, 2732-2753.

[55] B. Gates, B. Mayers, B. Cattle, Y. Xia, *Advanced Functional Materials*. **2002**, 12, 219-227.

[56] B. Mayers, Y. Xia, *Journal of Materials Chemistry*. **2002**, 12, 1875-1881.

[57] Q. Xie, Z. Dai, W. Huang, W. Zhang, D. Ma, X. Hu, Y. Qian, *Crystal growth & design*. **2006**, 6, 1514-1517.

[58] M. Mo, J. Zeng, X. Liu, W. Yu, S. Zhang, Y. Qian, *Advanced materials*. **2002**, 14, 1658-1662.

[59] Z. Wang, X. Chen, J. Liu, X. Yang, Y. Qian, *Inorganic Chemistry Communications*. **2003**, 6, 1329-1331.

[60] H.-S. Qian, S.-H. Yu, J.-Y. Gong, L.-B. Luo, L.-f. Fei, *Langmuir*. **2006**, 22, 3830-3835.

[61] B. Mayers, B. Gates, Y. Yin, Y. Xia, *Advanced materials*. **2001**, 13, 1380-1384.

[62] X. Jian, L. Yadong, *Materials chemistry and physics*. **2003**, 82, 515-519.

[63] W. Huang, Y. Zhang, Q. You, P. Huang, Y. Wang, Z.N. Huang, Y. Ge, L. Wu, Z. Dong, X. Dai, *Small*. **2019**, 15, 1900902.

[64] G. Xi, Y. Liu, X. Wang, X. Liu, Y. Peng, Y. Qian, *Crystal growth & design*. **2006**, 6, 2567-2570.

[65] Y.-t. Chen, W. Zhang, Y.-q. Fan, X.-q. Xu, Z.-x. Zhang, *Materials chemistry and physics*. **2006**, 98, 191-194.

[66] X. Jiang, L. Kemal, A. Yu, *Materials Letters*. **2007**, 61, 2584-2588.

[67] J.-M. Song, Y.-J. Zhan, A.-W. Xu, S.-H. Yu, *Langmuir*. **2007**, 23, 7321-7327.

[68] L. Ren, H. Zhang, P. Tan, Y. Chen, Z. Zhang, Y. Chang, J. Xu, F. Yang, D. Yu, *The Journal of Physical Chemistry B*. **2004**, 108, 4627-4630.

[69] X. Cao, Y. Xie, S. Zhang, F. Li, *Advanced Materials*. **2004**, 16, 649-653.

[70] Q. Wang, G.-D. Li, Y.-L. Liu, S. Xu, K.-J. Wang, J.-S. Chen, *The Journal of Physical*

Chemistry C. **2007**, 111, 12926-12932.

[71] N. Furuta, H. Itinose, N. Maruyama, Y. Ohasi, *Japanese Journal of Applied Physics*. **1972**, 11, 1113.

[72] X.-L. Li, G.-H. Cao, C.-M. Feng, Y.-D. Li, *Journal of Materials Chemistry*. **2004**, 14, 244-247.

[73] B. Geng, Y. Lin, X. Peng, G. Meng, L. Zhang, *Nanotechnology*. **2003**, 14, 983.

[74] C.J. Hawley, B.R. Beatty, G. Chen, J.E. Spanier, *Crystal growth & design*. **2012**, 12, 2789-2793.

[75] E. Filippo, D. Manno, A. Serra, *Crystal growth & design*. **2010**, 10, 4890-4897.

[76] C. Zhao, C. Tan, D.-H. Lien, X. Song, M. Amani, M. Hettick, H.Y.Y. Nyein, Z. Yuan, L. Li, M.C. Scott, *Nature Nanotechnology*. **2020**, 15, 53-58.

[77] Q. Wang, M. Safdar, K. Xu, M. Mirza, Z. Wang, J. He, *ACS nano*. **2014**, 8, 7497-7505.

[78] X. Zhang, J. Jiang, A.A. Suleiman, B. Jin, X. Hu, X. Zhou, T. Zhai, *Advanced Functional Materials*. **2019**, 29, 1906585.

[79] C. Lan, Z. Zhou, Z. Zhou, C. Li, L. Shu, L. Shen, D. Li, R. Dong, S. Yip, J.C. Ho, *Nano Research*. **2018**, 11, 3371-3384.

[80] K. Xia, V.I. Artyukhov, L. Sun, J. Zheng, L. Jiao, B.I. Yakobson, Y. Zhang, *Nano Research*. **2016**, 9, 2182-2189.

[81] C.M. Orofeo, S. Suzuki, H. Kageshima, H. Hibino, *Nano Research*. **2013**, 6, 335-347.

[82] Z. Lin, Y. Zhao, C. Zhou, R. Zhong, X. Wang, Y.H. Tsang, Y. Chai, *Scientific reports*. **2015**, 5, 1-10.

[83] X. Huang, J. Guan, Z. Lin, B. Liu, S. Xing, W. Wang, J. Guo, *Nano letters*. **2017**, 17, 4619-4623.

[84] H.O. Churchill, G.J. Salamo, S.-Q. Yu, T. Hironaka, X. Hu, J. Stacy, I. Shih, *Nanoscale research letters*. **2017**, 12, 488.

[85] Z. Yin, H. Li, H. Li, L. Jiang, Y. Shi, Y. Sun, G. Lu, Q. Zhang, X. Chen, H. Zhang, *ACS*

nano. **2012**, 6, 74-80.

[86] D. Wang, L.M. Tang, X.X. Jiang, J.Y. Tan, M.D. He, X.J. Wang, K.Q. Chen, *Advanced Electronic Materials*. **2019**, 5, 1800475.

[87] T. Furukawa, Y. Shimokawa, K. Kobayashi, T. Itou, *Nature communications*. **2017**, 8, 1-5.

[88] Y. Liu, W. Wu, W.A. Goddard III, *Journal of the American Chemical Society*. **2018**, 140, 550-553.

[89] Y. Zhao, J. Qiao, Z. Yu, P. Yu, K. Xu, S.P. Lau, W. Zhou, Z. Liu, X. Wang, W. Ji, *Advanced Materials*. **2017**, 29, 1604230.

[90] C. Zhou, Y. Zhao, S. Raju, Y. Wang, Z. Lin, M. Chan, Y. Chai, *Advanced functional materials*. **2016**, 26, 4223-4230.

[91] Y. Zhao, J. Qiao, P. Yu, Z. Hu, Z. Lin, S.P. Lau, Z. Liu, W. Ji, Y. Chai, *Advanced materials*. **2016**, 28, 2399-2407.

[92] H. Peng, N. Kioussis, G.J. Snyder, *Physical Review B*. **2014**, 89, 195206.

[93] S. Lin, W. Li, Z. Chen, J. Shen, B. Ge, Y. Pei, *Nature communications*. **2016**, 7, 1-6.

[94] S. Sharma, N. Singh, U. Schwingenschlögl, *ACS Applied Energy Materials*. **2018**, 1, 1950-1954.

[95] L.-B. Luo, X.-B. Yang, F.-X. Liang, J.-S. Jie, Q. Li, Z.-F. Zhu, C.-Y. Wu, Y.-Q. Yu, L. Wang, *CrystEngComm*. **2012**, 14, 1942-1947.

[96] Y. Zhao, K. Xu, F. Pan, C. Zhou, F. Zhou, Y. Chai, *Advanced Functional Materials*. **2017**, 27, 1603484.

[97] J. Wang, X. Guo, Z. Yu, Z. Ma, Y. Liu, M. Chan, Y. Zhu, X. Wang, Y. Chai, 2018 IEEE International Electron Devices Meeting (IEDM), IEEE2018, pp. 22.23. 21-22.23. 24.

[98] J. Yan, X. Zhang, Y. Pan, J. Li, B. Shi, S. Liu, J. Yang, Z. Song, H. Zhang, M. Ye, *Journal of Materials Chemistry C*. **2018**, 6, 6153-6163.

[99] T. Zhai, X. Fang, M. Liao, X. Xu, L. Li, B. Liu, Y. Koide, Y. Ma, J. Yao, Y. Bando, *Acs Nano*. **2010**, 4, 1596-1602.

[100] J. Xia, D. Zhu, L. Wang, B. Huang, X. Huang, X.M. Meng, *Advanced Functional Materials*. **2015**, 25, 4255-4261.

[101] Y. Chang, L. Chen, J. Wang, W. Tian, W. Zhai, B. Wei, *The Journal of Physical Chemistry C*. **2019**, 123, 21244-21251.

[102] M. Amani, C. Tan, G. Zhang, C. Zhao, J. Bullock, X. Song, H. Kim, V.R. Shrestha, Y. Gao, K.B. Crozier, *ACS nano*. **2018**, 12, 7253-7263.

[103] G. Qiu, S. Huang, M. Segovia, P.K. Venuthurumilli, Y. Wang, W. Wu, X. Xu, P.D. Ye, *Nano letters*. **2019**, 19, 1955-1962.

[104] M. Long, P. Wang, H. Fang, W. Hu, *Advanced Functional Materials*. **2019**, 29, 1803807.

[105] G. Liu, H. Wang, G.-L. Li, *Physics Letters A*. **2020**, 126431.

[106] Y.-Z. Chen, Y.-T. You, P.-J. Chen, D. Li, T.-Y. Su, L. Lee, Y.-C. Shih, C.-W. Chen, C.-C. Chang, Y.-C. Wang, *ACS applied materials & interfaces*. **2018**, 10, 35477-35486.

[107] K. Wu, H. Ma, Y. Gao, W. Hu, J. Yang, *Journal of materials chemistry A*. **2019**, 7, 7430-7436.

[108] J.K. Qin, G. Qiu, W. He, J. Jian, M.W. Si, Y.Q. Duan, A. Charnas, D.Y. Zemlyanov, H.Y. Wang, W.Z. Shao, *Advanced Functional Materials*. **2018**, 28, 1806254.

[109] J. Qin, H. Yan, G. Qiu, M. Si, P. Miao, Y. Duan, W. Shao, L. Zhen, C. Xu, D.Y. Peide, *Nano Research*. **2019**, 12, 669-674.

[110] H. Shang, H. Chen, M. Dai, Y. Hu, F. Gao, H. Yang, B. Xu, S. Zhang, B. Tan, X. Zhang, *Nanoscale Horizons*. **2020**, 5, 564-572.

[111] F. Qin, F. Gao, M. Dai, Y. Hu, M. Yu, L. Wang, P. Hu, W. Feng, *arXiv preprint arXiv:2001.07407*. **2020**.

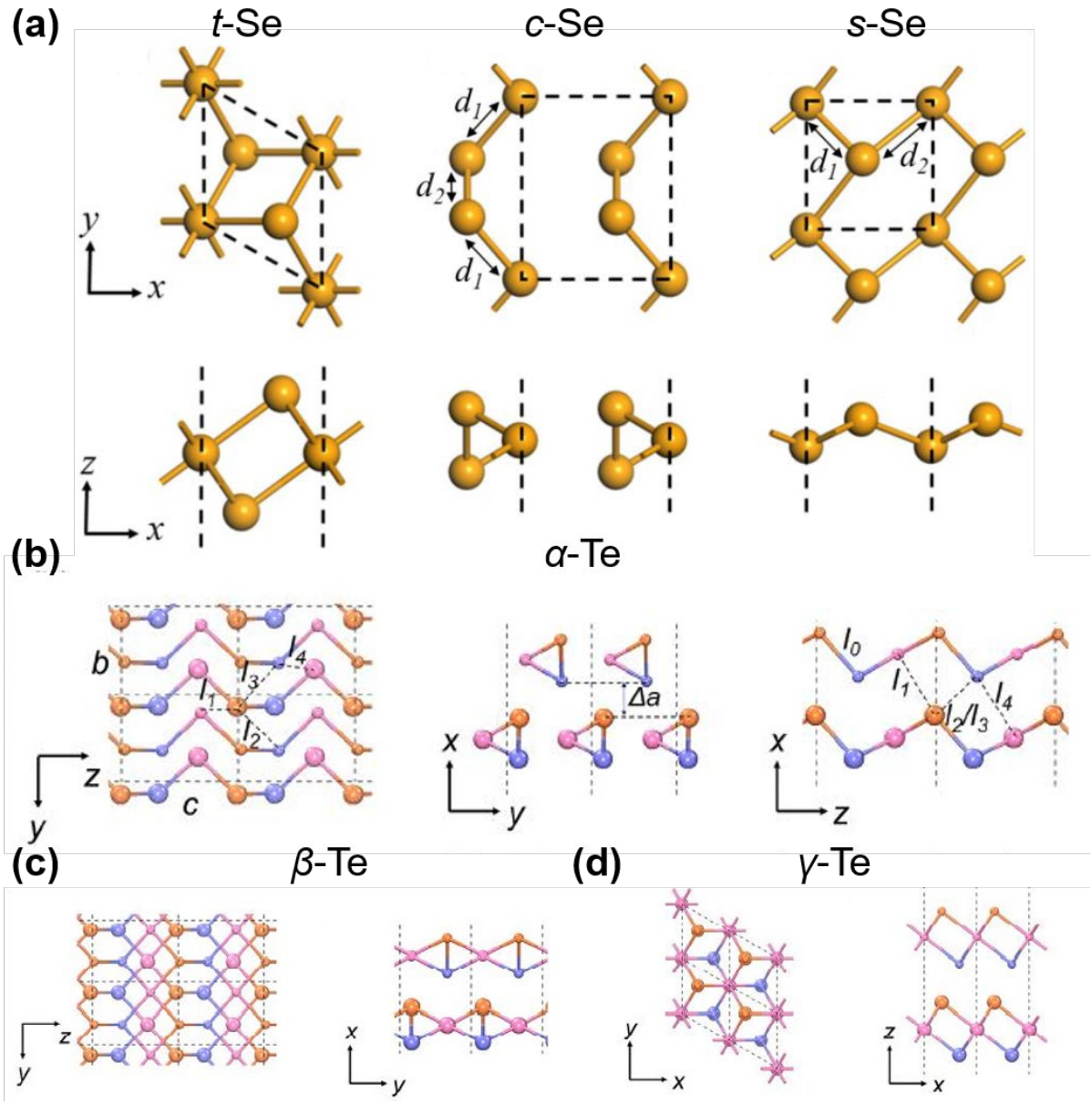

Figure 1. (a) Schematic top and side views of three structures of 2D Se: 1T-MoS_2-like structure (*t*-Se), tiled helical-chain structure (*c*-Se) and square structure (*s*-Se). Reproduced with permission.[42]. Copyright 2019, IOP Publishing Ltd. (b) Crystal structure of α-Te. (c) Top and side views of crystal structure of β-Te. (d) Top and side views of crystal structure of γ-Te. Reproduced with permission.[43] Copyright 2018, Science China Press.

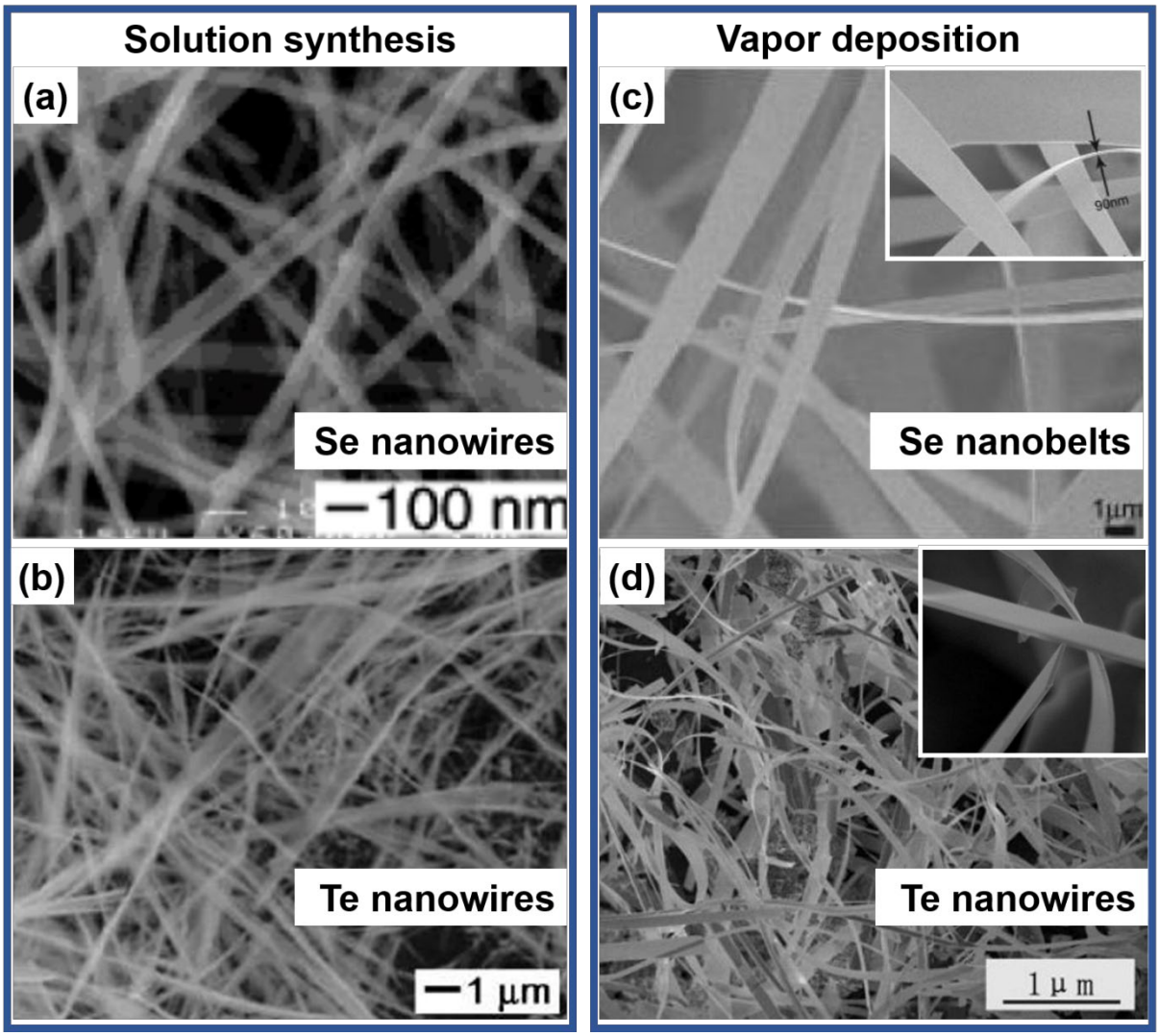

Figure 2. (a) SEM image of Se nanowires prepared by solution synthesis. Reproduced with permission.[55] Copyright 2002, WILEY-VCH Verlag GmbH, D-69469 Weinheim. (b) SEM image of Te nanowires prepared by solution synthesis. Inserted are SEM images with larger magnification. Reproduced with permission.[56] Copyright 2002, the Royal Society of Chemistry. (c) SEM image of Se nanobelts prepared by vapor deposition. Reproduced with permission.[70] Copyright 2007, American Chemical Society. (d) SEM image of Te nanobelts prepared by vapor deposition. Inserted are SEM images with larger magnification. Reproduced with permission.[73] Copyright 2003, IOP Publishing Ltd.

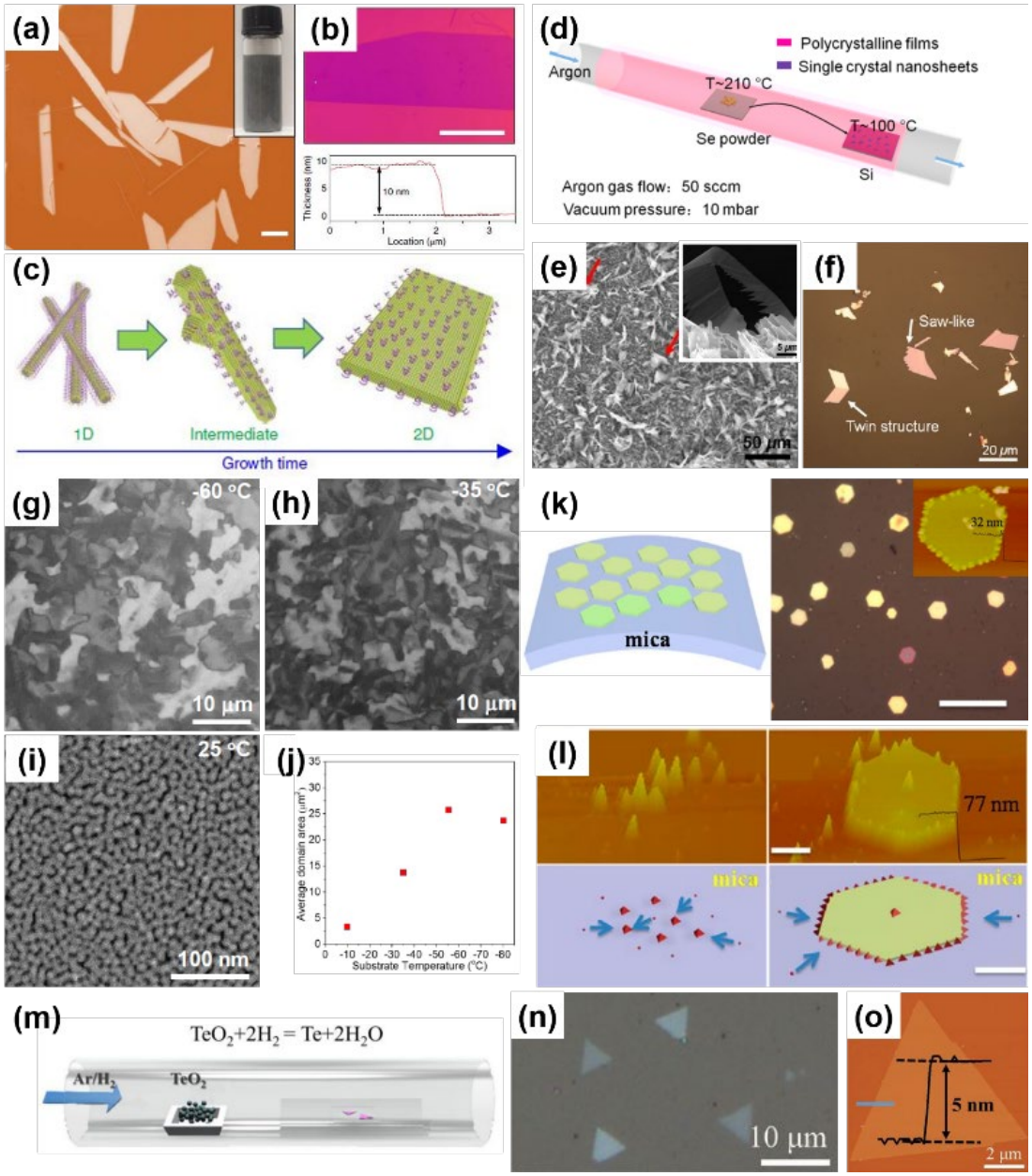

Figure 3. (a) to (c) Te thin flakes prepared by solution synthesis. (a) Optical image of Te flakes. Inserted is image of Te solution dispersion. (b) AFM image of a 10-nm-thick 2D Te flake. (c) Schematic of morphology evolution from 1D Te to 2D Te during the synthesis. Reproduced with permission.[45] Copyright 2018, Macmillan Publishers Limited, part of Springer Nature. (d) to (f) Se sheets prepared by PVD and post-growth transfer. (d) Schematic of the PVD method for Se sheets. (e) SEM image of as-grown Se sheets on the substrate. Inserted is SEM image of a typical Se sheet with saw-like structure. (f) Optical image of Se samples after the post-growth transfer. Reproduced with permission.[44] Copyright 2017, American Chemical Society. (g) to (j) Wafer-scale Te thin films grown by PVD. Polarized light microscopy images of Te thin films grown with different substrate temperatures (g) -60 ℃, (h) -35 ℃ and (i) 25 ℃. (J) The relationship between the average domain areas of Te thin films and substrate

temperatures. Reproduced with permission.[76] Copyright 2019, Springer Nature Limited. (k) and (l) Te plates grown by PVD. (k) Schematic of Te hexagonal plates on flexible mica substrates and optical image of 2D Te hexagonal plates. (l) Schematic for the growth process of 2D Te hexagonal plates with corresponding AFM images. Reproduced with permission.[77] Copyright 2014, American Chemical Society. (m) and (o) Te flakes grown by CVD. (m) Schematic of the CVD method for Te flakes. (n) Optical image of triangular Te thin flakes on mica substrates. (o) AFM image of a Te flake showing the ultrathin 5 nm thickness. Reproduced with permission.[78] Copyright 2019, WILEY-VCH Verlag GmbH & Co. KGaA, Weinheim.

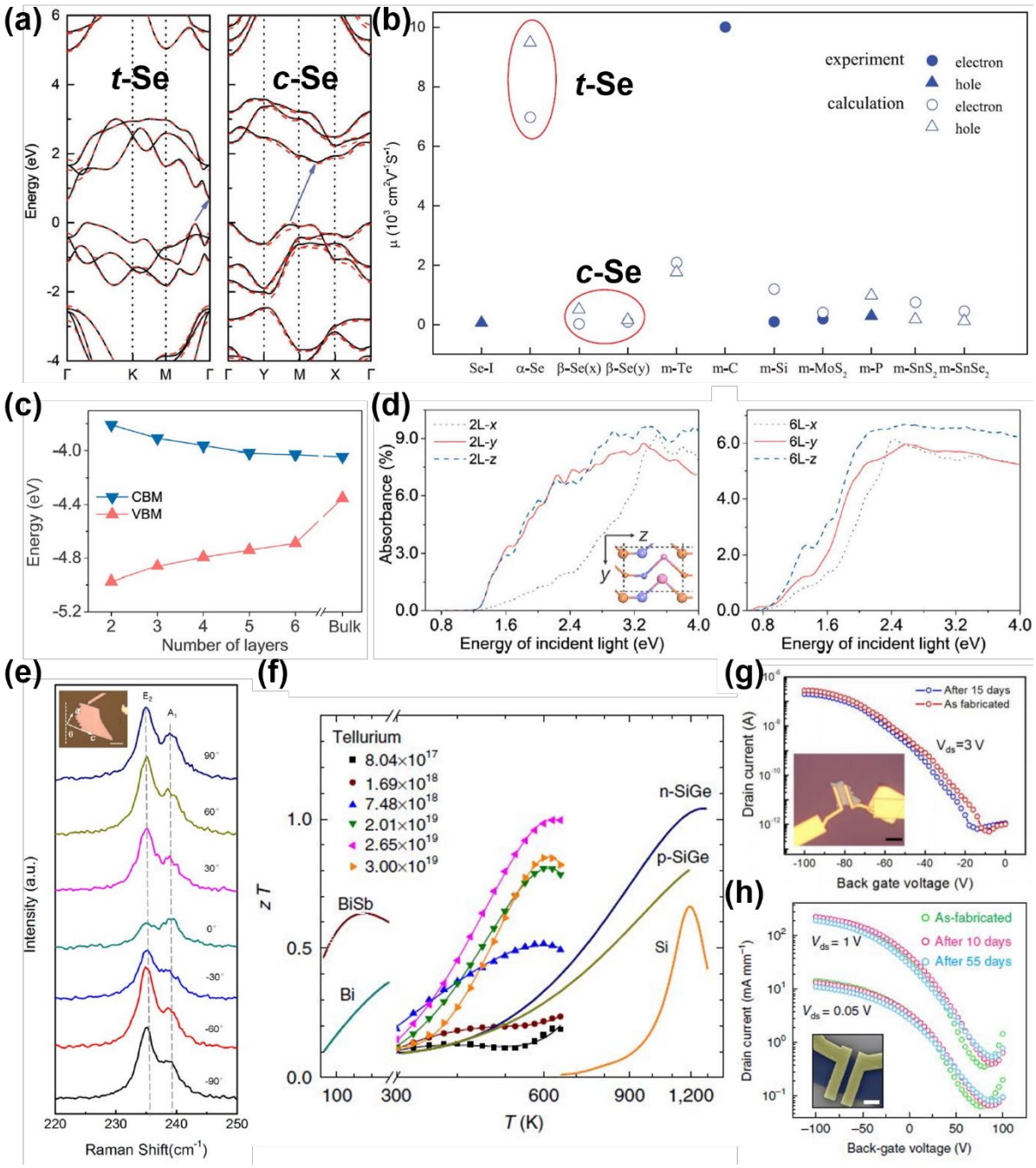

Figure 4. (a) Band structures of monolayer *t*-Se (1T-MoS_2-like structure) and *c*-Se (tiled helical-chain structure). (b) Comparison of the carrier mobility of monolayer Se with some conventional 2D materials. Reproduced with permission.[86] Copyright 2018, WILEY-VCH Verlag GmbH & Co. KGaA, Weinheim. (c) The positions of VBM and CBM in 2D Te related with Te thickness. (d) Optical absorption spectra of 2L- and 6L- α-Te with the polarized incident light along x, y, z directions in the crystal. Reproduced with permission.[43] Copyright 2018, Science China Press. (e) Angle-resolved Raman spectra of 2D Se related with angles between crystal orientation and incident laser polarization. Reproduced with permission.[44] Copyright 2017, American Chemical Society. (f) Temperature-dependent figure of merit (zT) for Te with different carrier concentrations, compared with other thermoelectric materials. Reproduced with permission.[93] Copyright Creative Commons Attribution 4.0 International License. (g) Transfer curves of a typical Se FET with stability measurement after 15-day air exposure. Reproduced with permission.[44] Copyright 2017, American Chemical Society. (h) Transfer curves of a typical Te FET with stability measurement after 55-day air exposure. Reproduced with permission.[45] Copyright 2018, Macmillan Publishers Limited, part of Springer Nature.

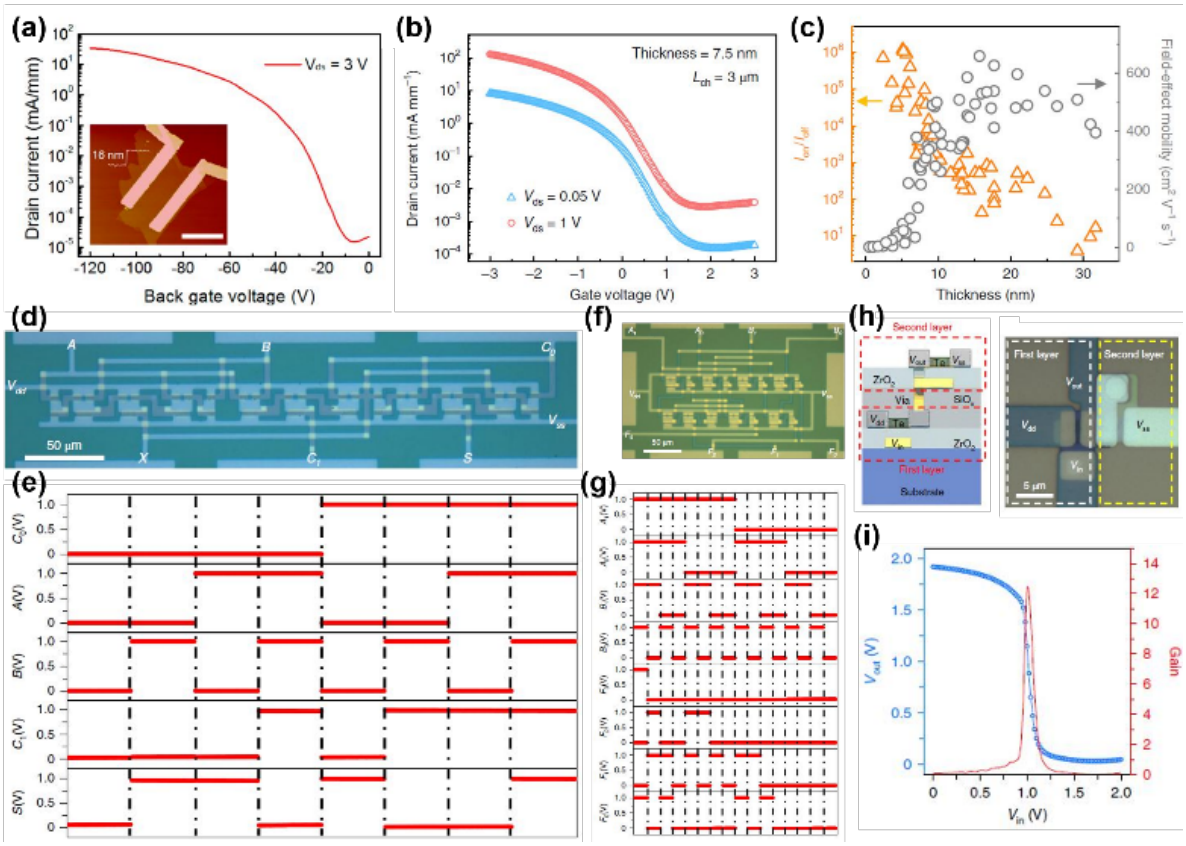

Figure 5. (a) Transfer curve of a typical FET based on Se nanosheet with the thickness of 16 nm. Inserted is AFM image of the device. Reproduced with permission.[44] Copyright 2017, American Chemical Society. (b) Transfer curves of a typical 2D Te FET with the thickness of

7.5 nm. (c) Thickness-dependent on/off ratio and field-effect mobility for 2D Te FETs. Reproduced with permission.[45] Copyright 2018, Macmillan Publishers Limited, part of Springer Nature. (d) and (e) Optical image and output voltage of a full-adder based on Te FETs. (f) and (g) Optical image and output voltage of a multiplier circuit based on Te FETs. (h) Schematic and optical image of a 3D inverter based on Te FETs. (i) The corresponding output voltage of the 3D inverter. Reproduced with permission.[76] Copyright 2019, Springer Nature Limited.

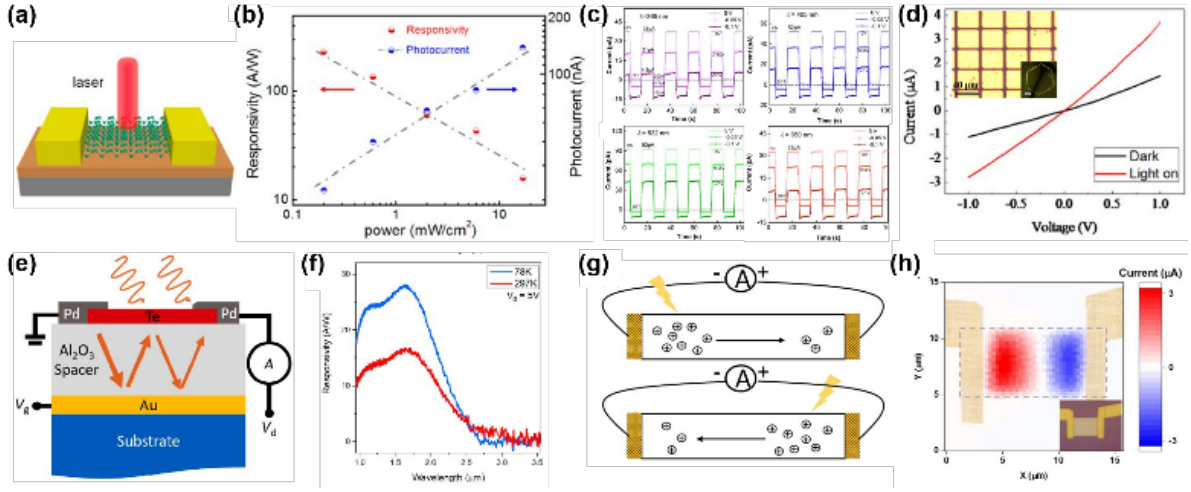

Figure 6. (a) Schematic of a phototransistor based on Se nanosheets. (b) The photocurrent and responsivity related with the laser illumination power at V_{ds} = 3 V and V_g = -80 V. Reproduced with permission.[44] Copyright 2017, American Chemical Society. (c) Time-dependent photo response of photodetectors based on Se microtubes with asymmetric contacts under 365, 405, 532, and 650 nm illumination at 0, -0.05, and -0.1 V bias. Reproduced with permission.[101] Copyright 2019, American Chemical Society. (d) I-V curves of photodetectors based on Te plates in the dark and under 473 nm laser. Inserted is optical image of the photodetectors. Reproduced with permission.[77] Copyright 2014, American Chemical Society. (e) Schematic of SWIR photoconductors based on 2D Te flakes with the optical cavity structure. (f) Photoresponsivity of the Te photoconductor measured at 78 and 297 K. Reproduced with permission.[102] Copyright 2018, American Chemical Society. (g) Schematic of photocurrent generation by thermoelectric effect of 2D Te. (h) The short circuit thermoelectric current mapping of photodetectors based on 2D Te. Reproduced with permission.[103] Copyright 2019, American Chemical Society.

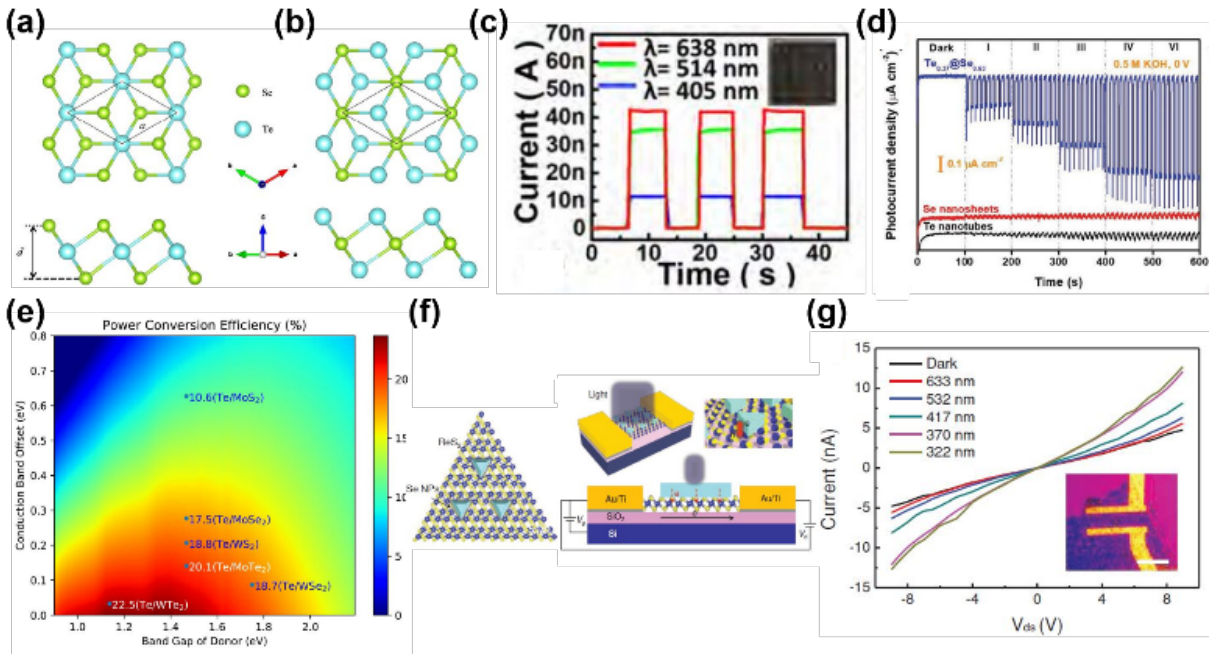

Figure 7. (a) Crystal structure of α-Se_2Te. (b) Crystal structure of α-$SeTe_2$. Reproduced with permission.[105] Copyright 2020, Elsevier B.V. (c) Time-dependent photo response of photodetectors based on 1D/2D hybrid structure of Se illuminated by 638, 514, and 405 nm wavelengths with the intensity of 0.3 mW/mm^2 and the bias voltage of 0.5 V. Reproduced with permission.[106] Copyright 2018, American Chemical Society. (d) Self-powered photo response of photodetectors based on Te nanotubes, Se nanosheets, and Se-Te junction in KOH solution. Reproduced with permission.[63] Copyright 2019, WILEY-VCH Verlag GmbH & Co. KGaA, Weinheim. (e) Diagram of power conversion efficiency of Te/TMDs heterojunction solar cells. Reproduced with permission.[107] Copyright 2019, the Royal Society of Chemistry. (f) Illustration of Se/ReS_2 heterostructure and schematic of the heterostructure photodetector. (g) Output curves of the phototransistors under different illumination wavelengths. Inserted is the optical image of the device. Reproduced with permission.[108] Copyright 2018, WILEY-VCH Verlag GmbH & Co. KGaA, Weinheim.

In this review, we introduce the crystal structures and preparation methods of group-VI elemental 2D materials, briefly review the electronic structures of group-VI 2D materials, and emphasize the device applications including transistors, photodetector and other emerging applications.

Keyword: group-VI 2D materials, crystal structures, preparations, electrical properties, nanoelectronics

Ziyuan Lin, Cong Wang, and Yang Chai*

Emerging Group-VI Elemental 2D Materials: Preparations, Properties and Device Applications